Extended quantitative rescattering model for simulating high-order harmonic streaking spectra by synchronization of an intense IR laser and a time-delayed attosecond XUV pulse

Kan Wang,[1] Baochang Li,[1] Xiangyu Tang,[1] Chenhui Xu,[1] C. D. Lin [ORCID],[2] and Cheng Jin [ORCID][1,*]

[1]*Department of Applied Physics, Nanjing University of Science and Technology, Nanjing, Jiangsu 210094, China*
[2]*J. R. Macdonald Laboratory, Department of Physics, Kansas State University, Manhattan, Kansas 66506, USA*

We theoretically investigate the modulated high-harmonic generation (HHG) driven by an intense few-cycle infrared (IR) laser field and a weak extreme-ultraviolet (XUV) pulse at a delayed time. We establish an extended quantitative rescattering (EQRS) model to simulate the HHG streaking spectra, with the ideas of correcting the IR ionization and the transition from the ground to continuum states in the strong-field approximation. The EQRS model has an accuracy comparable to that from "exactly" solving the time-dependent Schrödinger equation (TDSE). We reveal that the fringes in the streaking spectra are caused by the interference between the attosecond XUV pulse and harmonics resulting from different recombination pathways under the intense IR laser. We then demonstrate that the XUV pulse can be accurately retrieved by treating the single-atom TDSE results or macroscopic propagation results as the "input" data. This work provides with a tool for efficiently simulating and thoroughly analyzing the XUV-assisted HHG, which could also enhance its capability for tracing the electron dynamics involved in the strong-field phenomena.

I. INTRODUCTION

Laser-driven high-harmonic generation (HHG) has received continuous research interest in the past 30 years since the first observations at the end of 1980s [1,2]. HHG is fundamental to attosecond science [3–5] as it has become a reliable source for producing ultrashort attosecond light pulses in the form of attosecond pulse trains [6] or isolated attosecond pulses (IAPs) [7]. With the idea of restricting the efficient HHG emission occurring in a short time interval, various generation techniques have been developed to produce IAPs with durations of a few hundred to a few tens of attoseconds in the extreme ultraviolet (XUV) based on the traditional Ti:sapphire laser. These include amplitude gating [8], ionization gating [9], polarization gating [10], the attosecond lighthouse [11,12], multicolor wave-form synthesis [13–16], etc. Such attosecond XUV pulses provide a unique tool for probing the electron dynamics with time-resolved spectroscopy [17,18], initiating electron ionization [19,20], modifying the trajectory of an electron under an infrared (IR) laser [21], and so on.

The synchronization of attosecond XUV pulses and the IR laser has been widely used to perturb or to reform IR-generated HHG spectra by varying the time delay between the XUV pulse and IR laser. The XUV field was employed to populate the electron to the excited states or to select a specific electron trajectory by controlling the ionization step, thus greatly enhancing the yield of IR-induced HHG [22–24]. The HHG plateau by the IR laser was extended by the addition of a weak XUV pulse due to the XUV field-induced ac Stark modulations of the ground state [25]. The extension of the

HHG plateau can also be achieved by adding XUV pulses with higher photon energies, which enables the inner-shell electrons involved in the HHG process [26,27]. It has been shown that the interaction of the XUV field and IR laser can significantly influence one of three steps in the HHG process. If this interaction happens at the ionization step, the IR tunneling ionization is suppressed because the ionization energy of the target is effectively increased [28]. If this interaction occurs at the propagation step, multiple rescattering of the active electron can be induced, which is important for low-energy harmonics [29,30]. When the photon energy of the XUV pulse is far from the ionization threshold, it can be forward scattered from the nonstationary electronic wave packet promoted by the intense IR laser at the recombination step, thus leading to the parametric amplification of the XUV pulse, which has been extensively examined both experimentally and theoretically [31–39]. The XUV-assisted HHG has also been proposed to characterize attosecond pulses. For example, Xue *et al.* [40] theoretically investigated the dependence of the spectrum modulation on the chirp of the XUV under synchronized XUV and IR laser pulses, which could be useful for the reconstruction of the XUV spectral phase. Sarantseva *et al.* [41] proposed to retrieve the temporal intensity profile of an XUV attosecond pulse based on the XUV-assisted HHG by an intense IR pulse. Very recently, Dong *et al.* [42] found that interference fringe structures in the HHG streaking spectra can be used to observe the interplay of the photoionization and tunneling ionization electron dynamics at attosecond resolution. Sarantseva *et al.* [43] proposed a method for direct reconstruction of the HHG time-frequency spectrogram using time-delayed XUV-assisted HHG spectra.

In these studies, the HHG streaking spectra from the combination of an XUV pulse and an IR laser are usually

*cjin@njust.edu.cn

computed quantum mechanically by solving the time-dependent Schrödinger equation (TDSE) under the single-active electron (SAE) approximation [21,42,43] or by employing the formulation of a strong-field approximation (SFA) [29]. It is well known that TDSE can give precise results, but the physical mechanism has been hidden behind the numerical spectra. On the contrary, in the SFA the analytical formula can offer the physical meaning to describe the XUV-assisted HHG process, but it cannot simulate the spectra precisely. Therefore, the physical mechanism of XUV-assisted HHG remains insufficiently explored. It is necessary to develop new approaches to precisely simulate the HHG streaking spectra and to reveal the generation mechanism.

In this work, our main goal is to develop a theoretical method to accurately simulate the HHG streaking spectra. We choose a weak IAP with its central photon energy far from the ionization threshold of the target atom, which is used to modulate the continuum harmonic spectrum in the cutoff region generated by an intense few-cycle IR laser. The spectral modulation can be controlled by adjusting the time delay between the XUV and IR laser pulses. We will first separate the coupling between the XUV and IR pulses in the formulation of the SFA, and then we will extend and modify the well-established quantitative rescattering (QRS) model [44–46], which is valid for HHG from linearly polarized single- or multicolor IR laser pulses [47–49]. The calculated streaking spectra will be compared to those obtained by numerically solving the TDSE. Next, we will explain the interference fringes in the streaking spectra and uncover their physical origin. Then, we will demonstrate that by taking the TDSE results as "input" data or taking into account the macroscopic propagation effects, the HHG streaking spectra can be employed to recover the information from the input attosecond XUV pulse.

II. THEORETICAL METHODS

A. Separation of the contributions of IR and XUV pulses to the induced dipole in the strong-field approximation

We first use the SFA [29] to calculate the HHG streaking spectra under the linearly polarized XUV and intense IR laser pulses. The single-atom-induced dipole along the polarization direction at a fixed time delay τ between the two pulses can be expressed as

$$
\begin{aligned}
x(t, \tau) = i \int_0^t dt' \left(\frac{\pi}{\varepsilon + i(t - t')} \right)^{3/2} \\
\times d^*[p_{st}(t, t') - A(t)]e^{-iS_{st}(t,t')}d[p_{st}(t, t') - A(t')] \\
\times E(t') + \text{c.c.},
\end{aligned} \tag{1}
$$

where $E(t) = E_{IR}(t) + E_{XUV}(t - \tau)$ is the combined electric field of IR and XUV pulses and $A(t) = A_{IR}(t) + A_{XUV}(t - \tau)$ is the corresponding vector potential. Note that negative τ means the XUV pulse comes earlier than the peak of IR laser. Since the continuum state is treated as a plane wave, the dipole transition matrix element from the ground state to the continuum state can be expressed as

$$
d(p) = f(p)p, \tag{2}
$$

where p is the electron momentum and $f(p)$ is a complex function of p. Since the XUV laser is quite weak compared to the IR laser, to isolate the induced dipole using the IR laser alone, $E(t) \approx E_{IR}(t)$, and $f[p_{st} - A(t)] \approx f[p_{st} - A_{IR}(t)]$; thus, Eq. (1) can be expressed as

$$
\begin{aligned}
x(t, \tau) = i \int_0^t dt' \left(\frac{\pi}{\varepsilon + i(t - t')} \right)^{3/2} \\
\times f^*[p_{st}(t, t') - A_{IR}(t)]e^{-iS_{st}(t,t')} \\
\times f[p_{st}(t, t') - A_{IR}(t')] \\
\times [p_{st}(t, t') - A_{IR}(t) - A_{XUV}(t - \tau)] \\
\times [p_{st}(t, t') - A_{IR}(t') - A_{XUV}(t' - \tau)] \\
\times E_{IR}(t') + \text{c.c.},
\end{aligned} \tag{3}
$$

where p_{st} is the stationary momentum and S_{st} is the corresponding stationary action defined in the SFA [29]. The validity of Eq. (3) has been checked by comparing it with the HHG results from the standard SFA in Eq. (1).

To separate different processes in the time-dependent dipole, we rewrite $x(t, \tau)$ as

$$
x(t, \tau) = x_1(t) + x_2(t, \tau) + x_3(t, \tau) + x_4(t, \tau). \tag{4}
$$

Each term on the right-hand side of the equation can be explicitly expressed as follows:

$$
\begin{aligned}
x_1(t) = i \int_0^t dt' \left(\frac{\pi}{\varepsilon + i(t - t')} \right)^{3/2} \\
\times f^*[p_{st}(t, t') - A_{IR}(t)]e^{-iS_{st}(t,t')} \\
\times f[p_{st}(t, t') - A_{IR}(t')] \\
\times [p_{st}(t, t') - A_{IR}(t)][p_{st}(t, t') - A_{IR}(t')] \\
\times E_{IR}(t') + \text{c.c.},
\end{aligned} \tag{5}
$$

$$
\begin{aligned}
x_2(t, \tau) = -i \int_0^t dt' \left(\frac{\pi}{\varepsilon + i(t - t')} \right)^{3/2} \\
\times f^*[p_{st}(t, t') - A_{IR}(t)]e^{-iS_{st}(t,t')} \\
\times f[p_{st}(t, t') - A_{IR}(t')] \\
\times [p_{st}(t, t') - A_{IR}(t)]A_{XUV}(t' - \tau) \\
\times E_{IR}(t') + \text{c.c.},
\end{aligned} \tag{6}
$$

$$
\begin{aligned}
x_3(t, \tau) = -i \int_0^t dt' \left(\frac{\pi}{\varepsilon + i(t - t')} \right)^{3/2} \\
\times f^*[p_{st}(t, t') - A_{IR}(t)]e^{-iS_{st}(t,t')} \\
\times f[p_{st}(t, t') - A_{IR}(t')] \\
\times A_{XUV}(t - \tau)[p_{st}(t, t') - A_{IR}(t')] \\
\times E_{IR}(t') + \text{c.c.},
\end{aligned} \tag{7}
$$

and

$$
\begin{aligned}
x_4(t, \tau) = i \int_0^t dt' \left(\frac{\pi}{\varepsilon + i(t - t')} \right)^{3/2} \\
\times f^*[p_{st}(t, t') - A_{IR}(t)]e^{-iS_{st}(t,t')} \\
\times f[p_{st}(t, t') - A_{IR}(t')]
\end{aligned}
$$

$$\times A_{\mathrm{XUV}}(t - \tau)A_{\mathrm{XUV}}(t' - \tau)$$

$$\times E_{IR}(t') + \mathrm{c.c.} \tag{8}$$

Note that a formulation similar to Eq. (4) was used by Serrat *et al.* [32,33]. The limitation of the SFA for describing the single-atom response of HHG is well known. We will correct each term in Eq. (4) individually.

B. The QRS model for the dipole induced by the IR laser alone

The term $x_1(t)$ in Eq. (5) does not depend on the time delay τ. It can be rewritten as

$$x_1(t) = i \int_0^t dt' \left(\frac{\pi}{\varepsilon + i(t - t')}\right)^{3/2}$$

$$\times d^*[p_{st}(t, t') - A_{IR}(t)]e^{-iS_{st}(t,t')}d[p_{st}(t, t') - A_{IR}(t')]$$

$$\times E_{IR}(t') + \mathrm{c.c.} \tag{9}$$

This is the single-atom-induced dipole driven by the IR laser alone. In the frequency domain, according to the QRS model [50], it can be expressed as

$$x_1^{\mathrm{SFA}}(\omega, I) = N^{\mathrm{SFA}}(I)^{1/2}W_1(\omega)d^{\mathrm{SFA}}(\omega), \tag{10}$$

where $N^{\mathrm{SFA}}(I)$ and $d^{\mathrm{SFA}}(\omega)$ are the ionization probability (usually taken at the end of the IR laser pulse) and the transition dipole moment calculated within the SFA, respectively. Note that $d(\omega) = \langle 0|\vec{x}|p\rangle$, where $\omega = I_p + p^2/2$ (in atomic units), with electron position operator $\vec{x}$ (along laser polarization direction), ionization potential I_p, and wave functions of the ground state $|0\rangle$ and continuum states $|p\rangle$. The explicit expressions of $d^{\mathrm{SFA}}(\omega)$ are given in Eqs. (16) and (19). The dependence of the induced dipole on the peak intensity I of the IR laser has been given explicitly. In Eq. (10), the SFA can only give the correct electron wave packet $W_1(\omega)$ as

$$W_1(\omega) = \frac{x_1^{\mathrm{SFA}}(\omega, I)}{N^{\mathrm{SFA}}(I)^{1/2}d^{\mathrm{SFA}}(\omega)}; \tag{11}$$

thus, the QRS obtains the accurate induced dipole in the following:

$$x_1^{\mathrm{QRS}}(\omega, I) = x_1^{\mathrm{SFA}}(\omega, I)\frac{N^{\mathrm{QRS}}(I)^{1/2}}{N^{\mathrm{SFA}}(I)^{1/2}}\frac{d^{\mathrm{QRS}}(\omega)}{d^{\mathrm{SFA}}(\omega)}. \tag{12}$$

Here the ionization probability $N^{\mathrm{QRS}}(I)$ can be calculated by using the Perelomov-Popov-Terent'ev (PPT) model [51], and $d^{\mathrm{QRS}}(\omega)$ is computed by using the "exact" wave function for the bound and continuum states within the SAE approximation. The QRS model has been well established by calibrating against HHG results from TDSE calculations for atomic targets [46–48] and simple molecules [44,45,49]. The factorization of the induced dipole moment has also been derived analytically by others [52–55]. In this work, our target atom is Ne, and its model potential is given in Ref. [56].

C. Corrections of the XUV and IR coupling terms by extending the QRS model

For the $x_2(t, \tau)$ and $x_3(t, \tau)$ terms in Eq. (5), the interactions of the XUV pulse and IR laser with the atom are coupled. Similar to $x_1(\omega)$, in the frequency domain, $N(I)$ and $d(\omega)$ are the key factors to construct $x_2(\omega, \tau)$ and $x_3(\omega, \tau)$. Therefore,

we take advantage of the factorization idea in the QRS and write these terms at time delay τ in a similar way as

$$x_{2,3}^{\mathrm{SFA}}(\omega, I, \tau) = N^{\mathrm{SFA}}(I)^\alpha W_{2,3}(\omega, \tau)|d^{\mathrm{SFA}}(\omega)|^\beta, \tag{13}$$

where $W_{2,3}(\omega, \tau)$ are complex quantities similar to the electron wave packet in $x_1(\omega)$ and only depend on the external field. The parameters α and β are to be determined by fitting the SFA expressions. Once these parameters are known, $W_{2,3}(\omega, \tau)$ can be obtained, and accurate $x_2(\omega, \tau)$ and $x_3(\omega, \tau)$ are calculated by the extended quantitative rescattering (EQRS) model as

$$x_{2,3}^{\mathrm{EQRS}}(\omega, I, \tau) = x_{2,3}^{\mathrm{SFA}}(\omega, I, \tau)\frac{N^{\mathrm{QRS}}(I)^\alpha}{N^{\mathrm{SFA}}(I)^\alpha}\frac{|d^{\mathrm{QRS}}(\omega)|^\beta}{|d^{\mathrm{SFA}}(\omega)|^\beta}. \tag{14}$$

Since in Eq. (8) the term $A_{\mathrm{XUV}}(t - \tau)A_{\mathrm{XUV}}(t' - \tau)$ is much smaller than the terms of $[p_{st}(t, t') - A_{IR}(t)]A_{\mathrm{XUV}}(t' - \tau)$ and $A_{\mathrm{XUV}}(t - \tau)[p_{st}(t, t') - A_{IR}(t')]$ in $x_2(t, \tau)$ and $x_3(t, \tau)$, respectively, $x_4(t, \tau)$ is neglected in $x(t, \tau)$. Thus, in the EQRS model, the improved dipole induced by the XUV and IR pulses at a time delay τ can be computed from

$$x^{\mathrm{EQRS}}(\omega, I, \tau) = x_1^{\mathrm{QRS}}(\omega, I) + x_2^{\mathrm{EQRS}}(\omega, I, \tau)$$

$$+ x_3^{\mathrm{EQRS}}(\omega, I, \tau). \tag{15}$$

III. RESULTS AND DISCUSSION

A. The validity of the EQRS model for obtaining the HHG streaking spectra

1. The fitting procedure for determining the power factors in the EQRS model

In this work, we are interested in the spectral region where the XUV pulse overlaps with the high-order harmonics generated by the IR laser. To determine the power factors α and β in Eq. (13), we fit them from the calculated $x_{2,3}^{\mathrm{SFA}}(\omega, I, \tau)$. In the calculation, we treat Ne as a hydrogenlike atom. Then the transition dipole is given by

$$d(p) = i\frac{2^{7/2}(2I_p)^{5/4}}{\pi}\frac{p}{(p^2 + 2I_p)^3}, \tag{16}$$

where I_p is the ionization potential of Ne. We set time delay $\tau = 0$, the XUV pulse duration as 200 as, the central photon energy at 71.3 eV, and peak intensity at 5.0×10^{10} W/cm^2. The IR peak intensity is varied from 2.0 to 2.7×10^{14} W/cm^2. Other IR parameters are as follows: central wavelength of 800 nm, pulse duration of 5 fs (FWHM), carrier envelope phase (CEP) of zero, and a temporal profile described by a cosine-squared function. The simulated $|x_2^{\mathrm{SFA}}(\omega, I, \tau)|^2$ are shown in Fig. 1(a). The spectral shapes are similar, except that the peak values increase with intensity, reflecting the increase of the ionization probability. In Fig. 1(b), we plot the peak values as a function of the ionization probability $N^{\mathrm{SFA}}(I)$ (solid squares). By fitting these data to a power law, the obtained power factor is 0.26, which is close to 1/4. We thus set $\alpha = 1/8$ in Eq. (13). We next fix the intensity at 2.5×10^{14} W/cm^2 and vary the central energy of the XUV pulse from 62.0 to 83.7 eV. The calculated $|x_2^{\mathrm{SFA}}(\omega, I, \tau)|^2$ are plotted in Fig. 1(c). The shape of each spectrum is the same, but the peak value and central photon energy are different because of the shift of the central photon energy of the XUV pulse, which can
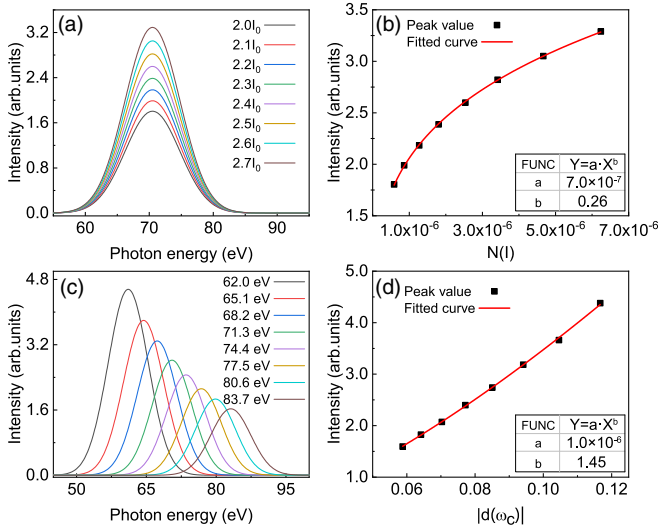
FIG. 1. (a) The spectra of $|x_2^{\mathrm{SFA}}(\omega, I, \tau)|^2$ calculated at different IR intensities indicated in units of I_0, where $I_0 = 10^{14}$ W/cm^2. The peak value is gradually increased with the increase of the IR intensity. (b) Their peak values (black squares) and the fitting curve (red line) as a function of $N(I)$. (c) The spectra of $|x_2^{\mathrm{SFA}}(\omega, I, \tau)|^2$ at different XUV central photon energies. The peak position coincides with the central energy of the XUV as labeled. (d) Their peak values (black squares) and the fitted curve (red line) with $|d(\omega_c)|$. The insets show the form of power-law fitting functions and the fitted parameters.

FIG. 2. The same as Fig. 1, except for calculating $|x_3^{\mathrm{SFA}}(\omega, I, \tau)|^2$.

be related to the photon-energy-dependent transition dipole moment. We apply the central momentum approximation; that is, $d(\omega)$ is replaced by $d(\omega_c)$, where ω_c is the XUV central photon energy. The peak values of $|x_2^{\mathrm{SFA}}(\omega, I, \tau)|^2$ are plotted as a function of $|d(\omega_c)|$ in Fig. 1(d). By fitting the curve to a power law, the power factor obtained is 1.45, which is close to 3/2, so we take $\beta = 3/4$. Using the same fitting procedure, we have checked that α and β do not change much with the time delay τ.

We use the same procedure to determine the α and β factors in $x_3^{\mathrm{SFA}}(\omega, I, \tau)$. By setting $\tau = 0$, plots similar to Fig. 1 are shown in Fig. 2. The fitted power factors are 0.25 and 0.85, or about 1/4 and 4/5 from Figs. 1 and 2. Thus, $\alpha = 1/8$, and $\beta = 2/5$ in Eq. (13). We have also checked that these parameters do not change with τ.

Thus, we obtain

$$x_2^{\mathrm{SFA}}(\omega, I, \tau) = N^{\mathrm{SFA}}(I)^{1/8} W_2(\omega, \tau) |d^{\mathrm{SFA}}(\omega)|^{3/4} \quad (17)$$

and

$$x_3^{\mathrm{SFA}}(\omega, I, \tau) = N^{\mathrm{SFA}}(I)^{1/8} W_3(\omega, \tau) |d^{\mathrm{SFA}}(\omega)|^{2/5}. \quad (18)$$

Equations (17) and (18) give the contribution of the XUV pulse to the induced dipole in the presence of the IR laser in the strong-field approximation. Note that there is no reemission of the XUV photon.

2. Comparison of HHG streaking spectra by using hydrogenlike and Gaussian atoms

To check the validity of the above fitting procedure, we also treat a Ne atom as a Gaussian potential. In this model, the
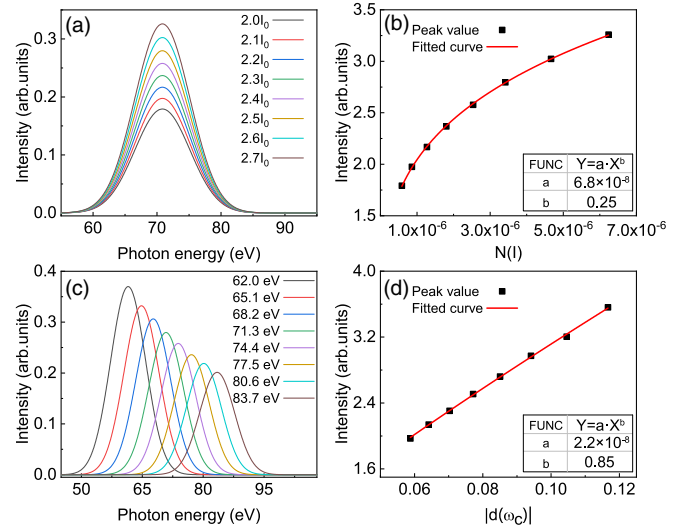
transition dipole moment is [29]

$$d(p) = i\left(\frac{1}{\pi\alpha}\right)^{3/4} \frac{p}{\alpha} e^{-p^2/2\alpha}, \quad (19)$$

where $\alpha = 0.7I_p$, with I_p being the ionization potential. We use the same IR and XUV parameters and the same fitting method; the obtained α and β factors are listed in Table I. One can see α match very well for the two different atomic systems, while the β values have some differences. Since ionization dominates the contribution to the transition dipole, the difference in β will not influence the final results of the induced dipole much.

We consider a 5-fs, 800-nm IR laser with a CEP of zero, and a peak intensity of 2.5×10^{14} W/cm^2. This pulse alone can produce high-order harmonics with a cutoff photon energy at about 70 eV. This IR laser is used throughout the rest of this paper unless otherwise stated. We consider a transform-limited (TL) XUV pulse with a duration of 200 as, central photon energy of 71.3 eV, and peak intensity of 5×10^{10} W/cm^2. At three time delays of 0, -20, and -40 as, the modulated harmonic spectra calculated using the EQRS model in Eq. (15) with two different atomic systems are shown in Fig. 3. Here the power spectrum is defined as being proportional to $\omega^4 |x^{\mathrm{EQRS}}(\omega, I, \tau)|^2$, in accordance with the acceleration gauge. One can see that in the spectral region of 55 to 65 eV, the two atomic systems give essentially the same spectra, and between 65 to 85 eV, they differ at most by a factor of 2 while the modulated spectral structures remain identical. This demonstrates that the expressions for

TABLE I. The fitted power factors, α and β, in $x_{2,3}(\omega, \tau)$ using different atomic models.

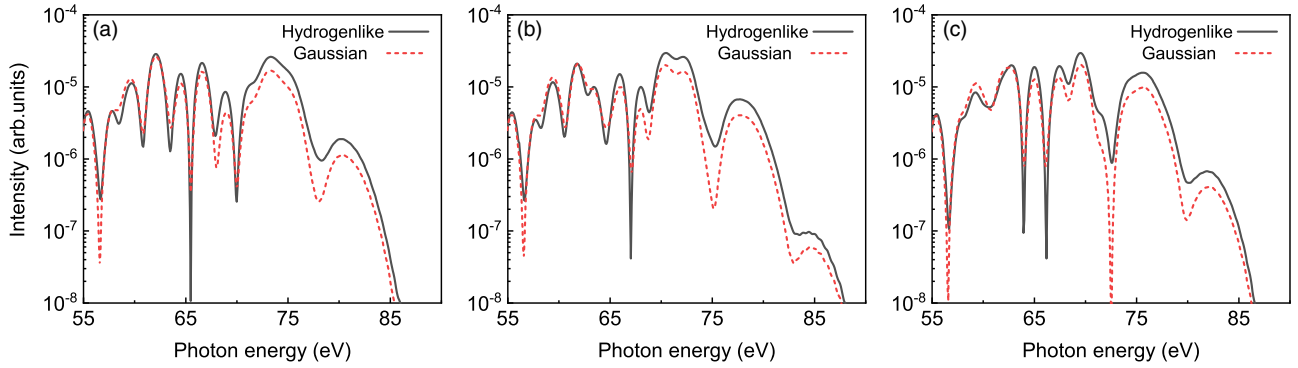| Atomic system	$x_2^{\mathrm{SFA}}(\omega, I, \tau)$		$x_3^{\mathrm{SFA}}(\omega, I, \tau)$	
	α	β	α	β
Hydrogenlike	1/8	3/4	1/8	2/5
Gaussian	1/8	1/2	1/8	1/4

FIG. 3. Comparison of HHG streaking spectra simulated by the EQRS model using hydrogenlike (black solid line) and Gaussian model (red dashed line) potentials for Ne. The spectra are shown at three selected time delays: (a) 0, (b) −20, and (c) −40 as.

$x_{2,3}^{\mathrm{SFA}}(\omega, I, \tau)$ in Eq. (13) are universal, and their dependence on the atomic system is quite weak.

B. Comparison of HHG streaking spectra with EQRS, SFA, and TDSE

We next take the same parameters as those in Fig. 3 and calculate the HHG streaking spectra by scanning the time delay from −0.5 to 0.5 fs using three methods: SFA, EQRS, and TDSE. The simulated results are shown in Fig. 4. In Figs. 4(a)–4(c), all three methods show the modulation versus time delay with a period of about 58 as, which is equal to one optical cycle of the XUV pulse. We also show the HHG streaking spectra obtained directly from the QRS model in Fig. 4(d) to express the necessity of its extension. For the distributions of spectral intensity versus the time delay, the EQRS results are much closer to the TDSE ones in comparison with the SFA ones. A detailed comparison of the four models can be seen in Figs. 4(e)–4(h) at four selected time delays. The EQRS can mostly reproduce the modulated HHG spectra by the TDSE over the spectral range of interest.

However, both the QRS and SFA fail in terms of the spectral shape and intensity. Here the TDSE results obtained with the SAE approximation with the model potential given in Ref. [56] are used to calibrate the EQRS model. The good agreement between them indeed shows the success of our approach for establishing the EQRS model. Note that we have checked that the HHG time-frequency spectrogram for neon in Ref. [43] can also be reproduced by using the EQRS model. Compared to solving the TDSE, the computation time of the EQRS model is greatly reduced and is nearly the same as the calculation time for the SFA. Thus, the EQRS model can be used to simulate the HHG streaking spectra. On the other hand, the EQRS model can also be utilized to understand the generation mechanism of XUV-assisted HHG.

C. Interpretation of interference fringes in the HHG streaking spectra

In the HHG streaking spectra, some interference fringes are present and, as an example, are replotted in Fig. 5(a) using the EQRS model. A black vertical line is drawn to
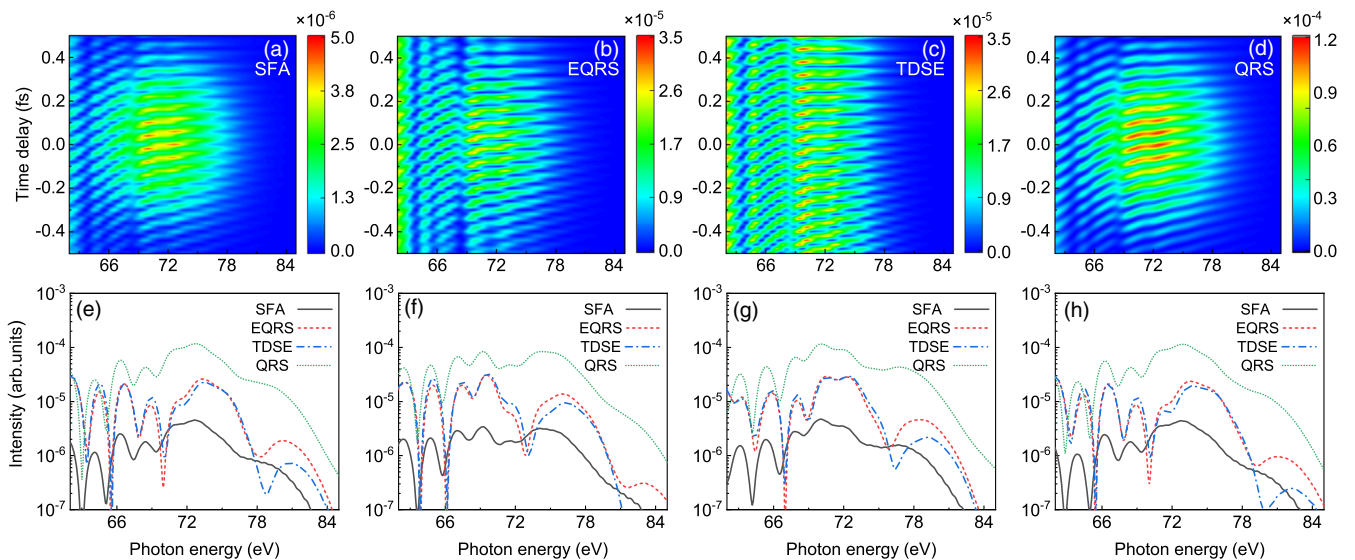

FIG. 4. The HHG streaking spectra calculated by four different methods: (a) SFA [black solid line in (e)–(h)], (b) EQRS (red dashed line), (c) TDSE (blue dot-dashed line), and (d) QRS (green dotted line). Comparison of the spectra obtained from the four methods at time delays of (e) 0, (f) 20, (g) 40, and (h) 60 as.
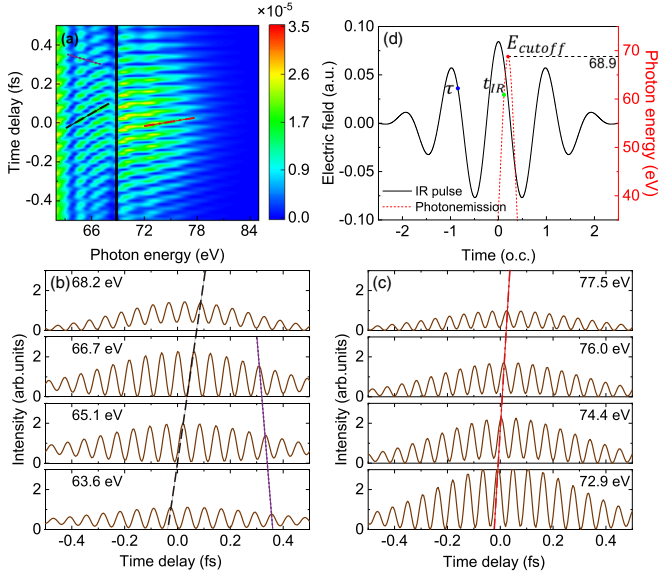
FIG. 5. (a) The HHG streaking spectra calculated by the EQRS model, replotted from Fig. 4(b). The vertical black solid line indicates the cutoff energy E_c of the IR laser, and the slopes of interference fringes are labeled by black dashed, purple dotted, and red dot-dashed lines. The delay-dependent intensity signals of the HHG spectra are shown (b) below and (c) above E_c. (d) The electric field of the IR laser (black solid line) and the harmonic emission time as a function of photon energy calculated by the classical trajectory model (red dotted line). t_{IR} is the harmonic emission time, and τ is the time delay between the XUV pulse and IR laser.

distinguish the regions of the three kinds of interference fringes, and they have different slopes that are labeled by a black dashed line, a purple dotted line, and a red dot-dashed line. The photon energy at the black vertical line is 68.9 eV, coincident with the cutoff energy of the HHG spectrum from the IR laser alone calculated using $E_c = I_p + 3.17U_p$, where I_p is the ionization potential and U_p is the ponderomotive energy. To reveal the origin of interference fringes, we make some assumptions based on the EQRS model, in which the XUV pulse interferes with the harmonics of the IR laser. According to Eq. (15), the intensity of the streaking spectra can be expressed as

$$S(\omega, \tau) = \left| x_1^{\text{QRS}}(\omega) + x_2^{\text{EQRS}}(\omega, \tau) + x_3^{\text{EQRS}}(\omega, \tau) \right|^2. \quad (20)$$

Since $x_1^{\text{QRS}}(\omega)$ is the dipole induced by the IR laser and $x_2^{\text{QRS}}(\omega)$ and $x_3^{\text{QRS}}(\omega)$ are the major and minor contributions to the total induced dipole from the XUV pulse coupled with the IR laser, respectively, we check that the amplitudes of $x_1^{\text{QRS}}(\omega)$ and $x_2^{\text{EQRS}}(\omega, \tau)$ are comparable in our simulations and the amplitude of $x_3^{\text{EQRS}}(\omega, \tau)$ is smaller than that of $x_2^{\text{EQRS}}(\omega, \tau)$, which can be neglected in the analysis. We thus have

$$S(\omega, \tau) \approx |A \exp[i\phi_1(\omega)] + A \exp[i\phi_2(\omega, \tau)]|^2, \quad (21)$$

where $\phi_1(\omega)$ is the spectral phase accumulated by the electron along a "short" or "long" trajectory under an intense IR laser and $\phi_2(\omega, \tau) = \omega\tau$ indicates the initial phase of the XUV pulse. Therefore, the modulation of the spectral intensity can

be written as

$$S^{\text{mod}}(\omega, \tau) \approx 2A^2 \cos[\omega\tau - \phi_1(\omega)]. \quad (22)$$

This equation indicates that $\phi_1(\omega)$ can be extracted from the modulated spectra. So the fringes in the HHG streaking spectra reflect the interference between the XUV pulse and different HHG pathways through the spectral phase. A time delay in photoemission can be defined as the group delay [57,58] from the derivative of the spectral phase, which is given by

$$\Delta G = \frac{d\phi_1(\omega)}{d\omega}. \quad (23)$$

We first extract the relative group delay from the HHG streaking spectra. As shown in Figs. 5(b) and 5(c), the peaks of the intensity signals at different energies are connected by straight lines, which help us to extract the relative group delays as

$$\Delta G = \frac{\omega_1\tau_1 - \omega_2\tau_2}{\omega_1 - \omega_2}, \quad (24)$$

where τ_1 and τ_2 are the time delays where the peaks appear for ω_1 and ω_2, respectively. For the photon-energy region of 63.6–68.2 eV, below the cutoff energy of E_c, the relative group delay is $\Delta G_{\text{below}} \approx 1.59$ and -0.60 fs for the black dashed and the purple dotted lines, respectively. However, $\Delta G_{\text{above}} \approx 0.49$ fs for photon energies of 72.9–77.5 eV, above the cutoff energy.

We can also calculate $d\phi_1(\omega)/d\omega$ in Eq. (23) by using the semiclassical three-step model. The electric field of the IR pulse (black solid line) is plotted in Fig. 5(d), and the harmonic emission times (red dotted line) as a function of photon energy for both short and long trajectories are calculated with the classical model. For cutoff harmonics, short and long trajectories are merged. The spectral phase $\phi_1(\omega)$ can be obtained as

$$\phi_1(\omega) = \omega t_{IR}, \quad (25)$$

with t_{IR} being the harmonic emission time. For photon energies of 63.3–68.2 eV, $d\phi_1(\omega)/d\omega$ is 2.11 and -1.03 fs for short and long trajectories, respectively, while it is 0.53 fs for cutoff harmonics in the photon-energy region of 72.9–77.5 eV.

From the agreement between ΔG extracted from the HHG streaking spectra and $d\phi_1(\omega)/d\omega$ calculated with the classical model, we can get the following conclusions. First, it confirms that the interference model based on the EQRS model is valid, in which the HHG streaking spectra are generated by the XUV pulse interfering with the harmonics of the IR laser. Second, it can also be concluded that the strong (weak) interference fringes [indicated by the black dashed line (purple dotted line) in Fig. 5(a)] in the HHG streaking spectra are caused by the interference between the XUV pulse and short-trajectory (long-trajectory) harmonics. The interference fringes above the cutoff energy are due to the interference between the XUV pulse and cutoff harmonics. Third, the interference fringes may be used to reconstruct the time-frequency picture of harmonic emission [43].
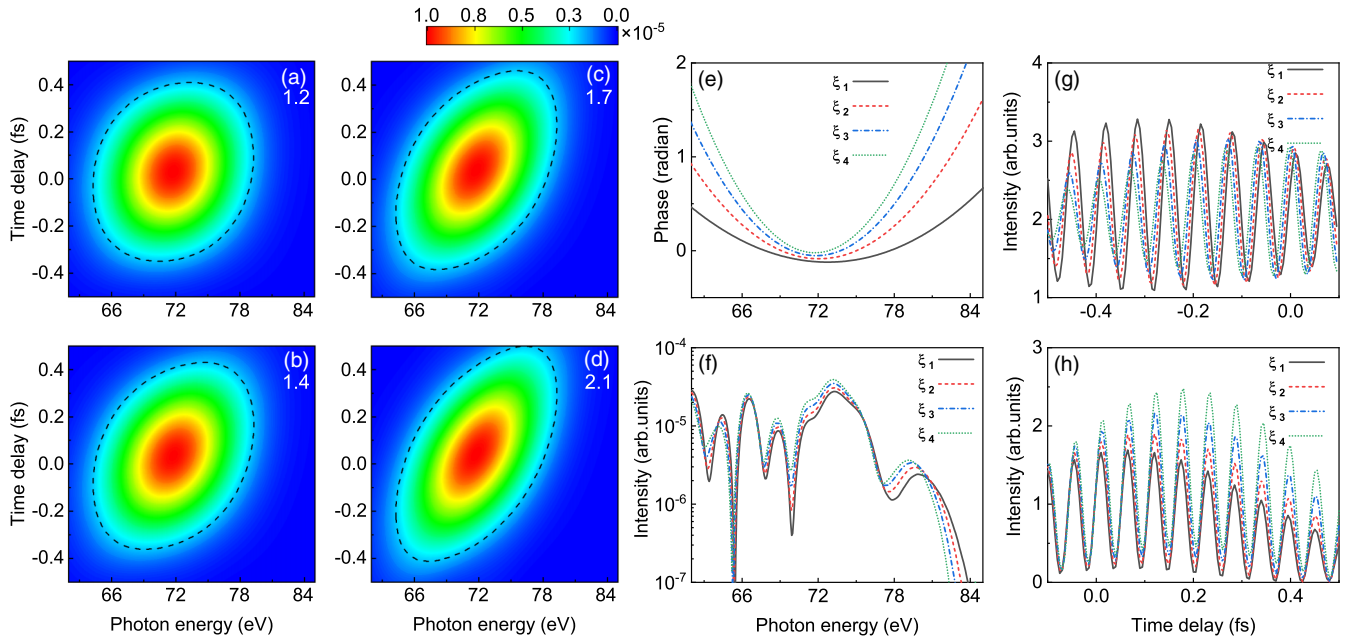
FIG. 6. The spectra of $|x_2^{\mathrm{EQRS}}(\omega, \tau) + x_3^{\mathrm{EQRS}}(\omega, \tau)|^2$ calculated by using the EQRS model with different spectral phases of the XUV pulse defined by the GDD (in atomic units): (a) $\xi_1 = -0.006$ [black solid line in (e)–(h)], (b) $\xi_2 = -0.012$ (red dashed line), (c) $\xi_3 = -0.018$ (blue dot-dashed line), and (d) $\xi_4 = -0.024$ (green dotted line). Black dotted lines are the contour lines which indicate 20% of the peak spectral intensity. (e) The phase of $x_2^{\mathrm{EQRS}}(\omega, \tau) + x_3^{\mathrm{EQRS}}(\omega, \tau)$ at zero time delay. (f) The HHG spectra including the interference with $x_1^{\mathrm{QRS}}(\omega)$ at zero time delay. The streaking spectra versus the time delay at two fixed photon energies: (g) 62 and (h) 76 eV.

D. Retrieval of the XUV pulse with the HHG streaking spectra using the EQRS model

1. Sensitivity of the HHG streaking spectra to the XUV spectral phase

The HHG streaking spectra may be used to retrieve the XUV pulse, or, more specifically, its spectral phase. We first need to check whether they are sensitive to the spectral phase of the XUV pulse. In the frequency domain, the XUV pulse can be expressed as $E_{\mathrm{XUV}}(\omega) = U(\omega)e^{i\phi(\omega)}$, where $U(\omega)$ is the spectral amplitude and $\phi(\omega)$ is the spectral phase. We start with the same TL XUV pulse as in Fig. 3. With the same $U(\omega)$, the phase $\phi(\omega)$ is given by $\phi(\omega) = \frac{\xi}{2}(\omega - \omega_c)^2$, where ω_c is the central photon energy and ξ is the coefficient of the group delay dispersion (GDD). In the EQRS model, the term of $x_1^{\mathrm{QRS}}(\omega)$ does not depend on the XUV pulse, so we check XUV-dependent terms of $x_2^{\mathrm{EQRS}}(\omega, \tau) + x_3^{\mathrm{EQRS}}(\omega, \tau)$ for completeness. We choose four different values of ξ and show the spectra of $|x_2^{\mathrm{EQRS}}(\omega, \tau) + x_3^{\mathrm{EQRS}}(\omega, \tau)|^2$ in Figs. 6(a)–6(d) (the normalization factor is indicated in each frame). It can clearly be seen that the spectra are very sensitive to the spectral phase of XUV pulse. We further show the phase of $x_2^{\mathrm{EQRS}}(\omega, \tau) + x_3^{\mathrm{EQRS}}(\omega, \tau)$ in Fig. 6(e) when the time delay is set to zero. The phase of the XUV-dependent terms changes rapidly with the XUV phase. We then include term of $x_1^{\mathrm{QRS}}(\omega)$ and check how the HHG streaking spectra vary with the XUV phase. In Fig. 6(f), the spectra are shown at zero time delay for four different XUV phases. The spectra change dramatically with the spectral phase. Similarly, as shown in Figs. 6(g) and 6(h), the intensities of harmonics at two energies show rapid modulations versus the time delay with a period of about 58 as for the XUV pulse. This strong dependence on the spectral

phase of the XUV makes the harmonic streaking spectra a good candidate for retrieving the XUV spectral phase.

2. Retrieval of the XUV pulse from the TDSE-based HHG streaking spectra

In the following we describe a general procedure for retrieving the spectral phase of the XUV pulse from the HHG streaking spectra. First, the XUV pulse and IR laser are characterized by a set of parameters $\{a_1, a_2, \ldots, a_n\}$. Second, for given ranges of photon energy and time delay, a fitness function is defined as

$$F\{a_i\} = \frac{\sum_{k,l}[S_0(\omega_k, \tau_l) - S_1(\omega_k, \tau_l)]^2}{N_k N_l}, \quad (26)$$

where S_0 are the input spectrograms and S_1 are the spectra simulated with the EQRS model using one set of $\{a_1, a_2, \ldots, a_n\}$. N_k and N_l are the numbers of data points for the photon energy and the time delay, respectively. Third, multiple parameters can be searched and determined by minimizing $F\{a_i\}$.

The purpose of this work is to demonstrate the applicability of the HHG streaking spectra for characterizing the XUV pulse. Since the IR laser alone is strong enough to generate high-order harmonics, it can be characterized independently with the generated HHG spectra. The spectral intensity of the XUV pulse can easily be measured with a spectrometer. We assume that the IR laser and the spectral intensity of the XUV are known, and the spectral phase is characterized by the GDD coefficient ξ; that is, the XUV pulse is characterized by a single parameter. For different values of ξ, the HHG streaking spectra calculated using the TDSE are shown in
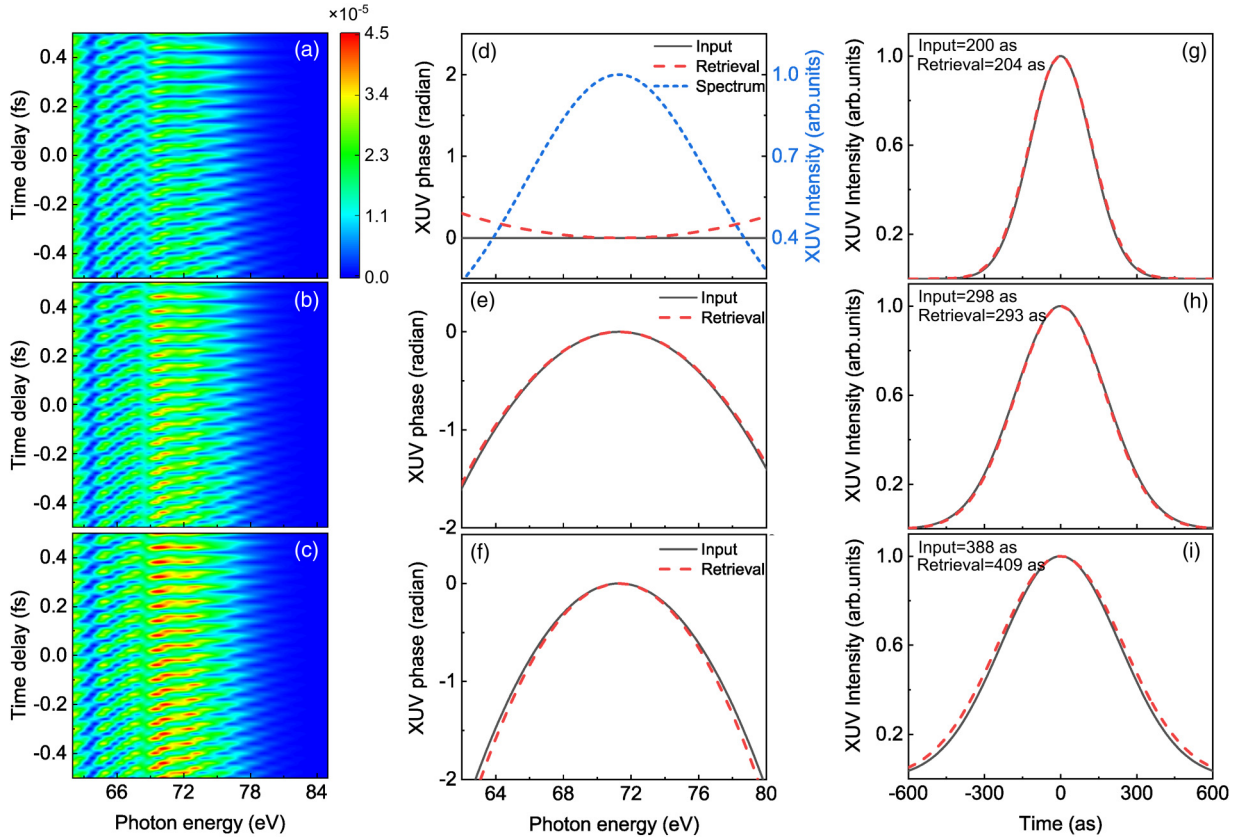
FIG. 7. Characterization of three XUV pulses centered at 71.3 eV with a bandwidth of 9 eV. The GDD coefficients ξ (in atomic units) of these XUV pulses are 0 (first row), -0.016 (second row), and -0.024 (third row). (a)–(c) The input modulated spectra simulated by the TDSE are treated as experimental data. (d)–(f) Comparison of the input and retrieved spectral phases. (g)–(i) Comparison of the input and retrieved XUV intensity profiles in time domain. (The black solid lines are the input data, while the red dashed lines are retrieved results.) The spectral intensity $U(\omega)^2$ of the XUV pulse (blue dotted line) is assumed to be known, as shown in (d).

Figs. 7(a)–7(c). The spectrograms are significantly changed by varying the XUV spectral phase. These data are used as input data or "experimental" data that we want to fit. We then search the optimized ξ until $F\{a_i\}$ is minimized. In the retrieval procedure, we typically choose 100 points in the time delay and 300 points in the photon energy. The retrieved spectral phases are plotted (red dashed lines) in Figs. 7(d)–7(f). For comparison, the input phases are also shown (black solid lines). To evaluate the accuracy of the retrieved results, we plot the XUV intensity profiles in the time domain in Figs. 7(g)–7(i). For the TL pulse, our method gives a pulse duration (FWHM) of 205 as, in comparison to the input value of 200 as in Fig. 7(g). As the absolute values of ξ are increased, the retrieved (input) durations are 293 as (298 as) and 409 as (388 as) in Figs. 7(h) and 7(i), respectively. All input XUV pulse durations can be successfully retrieved with a relative error less than 5%.

3. Retrieval of XUV pulses from macroscopic HHG streaking spectra

In the above retrieval procedure, the input data are taken from the single-atom response. In reality, the experimentally measured HHG spectra undergo change from the macroscopic

phase-matching effects as the light emerges from the gas medium [59–66]. Our retrieval method needs to be checked with experimental HHG streaking spectra which depend on the focusing conditions. Instead of accounting for good phase matching when the gas medium is placed after the laser focus by solving the three-dimensional Maxwell wave equation [67], an easier shortcut to get the same result is to average the single-atom complex harmonic amplitudes over a narrow intensity range of the IR pulse. We have used such a simplified procedure by averaging over a range $[0.95I_c, 1.05I_c]$ around the central intensity I_c, where $I_c = 2.5 \times 10^{14}$ W/cm^2. Note that the average was taken coherently and the XUV pulse was not varied since its Rayleigh length is much longer than that of the IR laser. The resulting experimental streaking HHG spectra are shown in Fig. 8(a). For simplicity, S_1 in Eq. (26) are still given by the single-atom spectra calculated with the EQRS model. With the known XUV spectral intensity and the IR laser of intensity I_c, we use the same single-parameter retrieval method to obtain the XUV spectral phase and thus the XUV pulse. Using the retrieved XUV pulse, we can calculate the streaking spectra, as shown in Fig. 8(b), which compares nicely with the input one shown in Fig. 8(a). The retrieved XUV spectral phase and temporal intensity profile are plotted in Figs. 8(c) and 8(d), respectively. The retrieved pulse duration is 308 as, which compares well with the input value
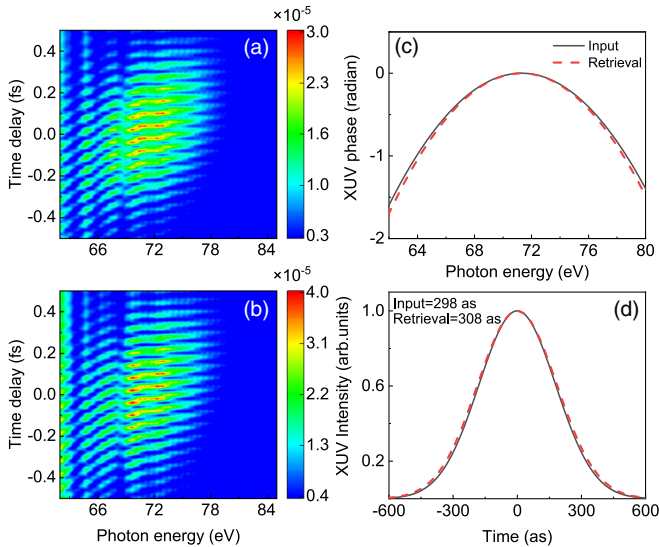
FIG. 8. (a) The HHG streaking spectra after accounting for the propagation effects by averaging IR intensities (input). The GDD coefficient ξ (in atomic units) is -0.016. (b) The retrieved modulation spectra using the single-atom theory. Comparison of (c) the retrieved XUV spectral phase and (d) the temporal intensity profile.

of 298 as. This shows that macroscopic propagation of the harmonic spectra does not alter the essential features in the single-atom HHG streaking spectra.

IV. CONCLUSIONS

In summary, we have established an extended quantitative rescattering model to accurately and efficiently simulate the HHG streaking spectra generated by the combination of a linearly polarized weak XUV pulse and an intense IR laser. In this model, the induced dipole caused by the IR laser alone can be calculated using the standard QRS model, while the time-delay-dependent IR-XUV coupling terms can be corrected by considering the contributions from the IR-laser ionization and the bound-continuum transition. The consistence of this model was checked by treating the target atom as a hydrogenlike or a Gaussian atom in the SFA. The EQRS model was also calibrated by comparing it with the results obtained

from the TDSE solutions. Next, we uncovered the physical mechanism of the fringes in the HHG streaking spectra, which are caused by the interference between the XUV pulse and harmonics of the IR laser. The harmonics generated by the short or long electron trajectory or above the cutoff are responsible for interference fringes with different slopes. Then we examined whether the HHG streaking spectra are sensitive to the XUV spectral phase, thus nicely forming the basis for the retrieval. Finally, we demonstrated that the spectral phase of the XUV pulse can be retrieved with the present method by using input HHG spectra generated from solving the TDSE, and the result remains the same even if the phase matching in the macroscopic gas medium is included.

In this work, the central photon energy of the XUV pulse was chosen to be far from the ionization threshold of a target atom, and the pulse duration was about a few hundred attoseconds. The applicability of the EQRS model needs to be further checked for a wide parameter range of the XUV pulse. Recently, with the development of laser technology in the midinfrared, several groups have reported continuum harmonic spectra in the water window or soft x-ray (SXR) region [68–71]; it is also interesting to check whether the EQRS model can be used to simulate the HHG streaking spectra using the synchronization of an attosecond SXR pulse and a midinfrared laser. In the present retrieval, we simulated the case where there is only one unknown parameter. If multiple parameters are required to characterize both the XUV pulse and IR laser, optimization algorithms [72,73] should be applied to speed up the process of searching optimal parameters. In addition, the retrieval of a broadband soft x-ray IAP generated with mid-IR lasers is also appealing, and the capability of the present retrieval method will be explored in the future.

[1] A. McPherson, G. Gibson, H. Jara, U. Johann, T. S. Luk, I. A. McIntyre, K. Boyer, and C. K. Rhodes, J. Opt. Soc. Am. B **4**, 595 (1987).

[2] M. Ferray, A. L'Huillier, X. F. Li, L. A. Lompre, G. Mainfray, and C. Manus, J. Phys. B **21**, L31 (1988).

[3] F. Calegari, G. Sansone, S. Stagira, C. Vozzi, and M. Nisoli, J. Phys. B **49**, 062001 (2016).

[4] L.-Y. Peng, W.-C. Jiang, J.-W. Geng, W.-H. Xiong, and Q. Gong, Phys. Rep. **575**, 1 (2015).

[5] F. Krausz and M. Ivanov, Rev. Mod. Phys. **81**, 163 (2009).

[6] P. M. Paul, E. S. Toma, P. Breger, G. Mullot, F. Augé, P. Balcou, H. G. Muller, and P. Agostini, Science **292**, 1689 (2001).

[7] M. Hentschel, R. Kienberger, C. Spielmann, G. A. Reider, N. Milosevic, T. Brabec, P. Corkum, U. Heinzmann, M. Drescher, and F. Kraus, Nature (London) **414**, 509 (2001)

[8] E. Goulielmakis, M. Schultze, M. Hofstetter, V. S. Yakovlev, J. Gagnon, M. Uiberacker, A. L. Aquila, E. M. Gullikson, D. T. Attwood, R. Kienberger, F. Krausz, and U. Kleineberg, Science **320**, 1614 (2008).

[9] A. Jullien, T. Pfeifer, M. J. Abel, P. M. Nagel, M. J. Bell, D. M. Neumark, and S. R. Leon, Appl. Phys. B **93**, 433 (2008).

[10] I. J. Sola, E. Mével, L. Elouga, E. Constant, V. Strelkov, L. Poletto, P. Villoresi, E. Benedetti, J. P. Caumes, S. Stagira, C. Vozzi, G. Sansone, and M. Nisoli, Nat. Phys. **2**, 319 (2006).

[11] H. Vincenti and F. Quéré, Phys. Rev. Lett. **108**, 113904 (2012).

[12] K. T. Kim, C. M. Zhang, T. Ruchon, J. F. Hergott, T. Auguste, D. M. Villeneuve, P. B. Corkum, and F. Quéré, Nat. Photonics **7**, 651 (2013).

[13] S. W. Huang, G. Cirmi, J. Moses, K. H. Hong, S. Bhardwaj, J. R. Birge, L. J. Chen, E. Li, B. J. Eggleton, G. Cerullo, and F. X. Kärtner, Nat. Photonics **5**, 475 (2011).

[14] D. Greening, B. Weaver, A. J. Pettipher, D. J. Walke, E. W. Larsen, J. P. Marangos, and J. W. G. Tisch, Opt. Express **28**, 23329 (2020).

[15] E. J. Takahashi, P. F. Lan, O. D. Mücke, Y. Nabekawa, and K. Midorikawa, Nat. Commun. **4**, 2691 (2013).

[16] B. Xue, Y. Tamaru, Y. Fu, H. Yuan, P. F. Lan, O. D. Mücke, A. Suda, K. Midorikawa, and E. J. Takahas, Sci. Adv. **6**, eaay2802 (2020).

[17] Y. Pertot, C. Schmidt, M. Matthews, A. Chauvet, M. Huppert, V. Svoboda, A. von Conta, A. Tehlar, D. Baykusheva, J. P. Wolf, and H. J. Wörner, Science **355**, 264 (2017).

[18] A. Ozawa, J. Rauschenberger, C. Gohle, M. Herrmann, D. R. Walker, V. Pervak, A. Fernandez, R. Graf, A. Apolonski, R. Holzwarth, F. Krausz, T. W. Hänsch, and T. Udem, Phys. Rev. Lett. **100**, 253901 (2008).

[19] C. Buth, F. He, J. Ullrich, C. H. Keitel, and K. Z. Hatsagortsyan, Phys. Rev. A **88**, 033848 (2013).

[20] M. R. Miller, C. Hernández-García, A. Jaroń-Becker, and A. Becker, Phys. Rev. A **90**, 053409 (2014).

[21] C. Liu, Z. Zeng, R. Li, Z. Xu, and M. Nisoli, Opt. Express **23**, 9858 (2015).

[22] C. Figueira de Morisson Faria, P. Salières, P. Villain, and M. Lewenstein, Phys. Rev. A **74**, 053416 (2006).

[23] K. J. Schafer, M. B. Gaarde, A. Heinrich, J. Biegert, and U. Keller, Phys. Rev. Lett. **92**, 023003 (2004).

[24] G.-T. Zhang, J. Wu, C.-L. Xia, and X.-S. Liu, Phys. Rev. A **80**, 055404 (2009).

[25] A. Fleischer, Phys. Rev. A **78**, 053413 (2008).

[26] A. C. Brown and H. W. van der Hart, Phys. Rev. Lett. **117**, 093201 (2016).

[27] J.-A. You, J. M. Dahlström, and N. Rohringer, Phys. Rev. A **95**, 023409 (2017).

[28] N. B. Delone, N. L. Manakov, and A. G. Fainshtein, Sov. Phys. JETP **59**, 529 (1984).

[29] M. Lewenstein, P. Balcou, M. Y. Ivanov, A. L'Huillier, and P. B. Corkum, Phys. Rev. A **49**, 2117 (1994).

[30] T. S. Sarantseva, M. V. Frolov, and N. V. Vvedenskii, Quantum Electron. **48**, 625 (2018).

[31] J. Seres, E. Seres, B. Landgraf, B. Ecker, B. Aurand, A. Hoffmann, G. Winkler, S. Namba, T. Kuehl, and C. Spielmann, Sci. Rep. **4**, 04254 (2014).

[32] C. Serrat, D. Roca, and J. Seres, Opt. Express **23**, 4867 (2015).

[33] C. Serrat, D. Roca, J. M. Budesca, J. Seres, E. Seres, B. Aurand, A. Hoffmann, S. Namba, T. Kuehl, and C. Spielmann, Opt. Express **24**, 8028 (2016).

[34] J. Seres, E. Seres, D. Hochhaus, B. Ecker, D. Zimmer, V. Bagnoud, T. Kuehl, and C. Spielmann, Nat. Phys. **6**, 455 (2010).

[35] J. Seres, E. Seres, and C. Spielmann, Phys. Rev. A **86**, 013822 (2012).

[36] C. Serrat, Phys. Rev. Lett. **111**, 133902 (2013).

[37] J. Seres, E. Seres, B. Landgraf, B. Ecker, B. Aurand, T. Kuehl, and C. Spielmann, Sci. Rep. **4**, 04234 (2014).

[38] C. Serrat, J. Seres, E. Seres, and S. Namba, Phys. Rev. A **99**, 063425 (2019).

[39] C. Serrat, Phys. Rev. A **93**, 063415 (2016).

[40] J. Xue, C. Liu, Y. Zheng, Z. Zeng, R. Li, and Z. Xu, Opt. Express **26**, 9243 (2018).

[41] T. S. Sarantseva, M. V. Frolov, N. L. Manakov, A. A. Silaev, A. A. Romanov, N. V. Vvedenskii, and A. F. Starace, Phys. Rev. A **101**, 013402 (2020).

[42] W. Dong, H. Hu, and Z. Zhao, Opt. Express **28**, 22490 (2020).

[43] T. S. Sarantseva, A. A. Silaev, A. A. Romanov, N. V. Vvedenskii, and M. V. Frolov, Opt. Express **29**, 1428 (2021).

[44] A.-T. Le, R. R. Lucchese, S. Tonzani, T. Morishita, and C. D. Lin, Phys. Rev. A **80**, 013401 (2009).

[45] C. D. Lin, A.-T. Le, C. Jin, and H. Wei, J. Phys. B **51**, 104001 (2018).

[46] T. Morishita, A.-T. Le, Z. Chen, and C. D. Lin, Phys. Rev. Lett. **100**, 013903 (2008).

[47] A.-T. Le, T. Morishita, and C. D. Lin, Phys. Rev. A **78**, 023814 (2008).

[48] S.-F. Zhao, Y. Wang, G. Wang, and X.-X. Zhou, Opt. Commun. **328**, 30 (2014).

[49] A.-T. Le, R. D. Picca, P. D. Fainstein, D. A. Telnov, M. Lein, and C. D. Lin, J. Phys. B **41**, 081002 (2018).

[50] N. Abro, K. Wang, X. Zhu, B. Li, and C. Jin, Phys. Rev. A **98**, 023411 (2018).

[51] A. M. Perelomov, V. S. Popov, and M. V. Terent'ev, Sov. Phys. JETP **23**, 924 (1966).

[52] M. V. Frolov, N. L. Manakov, T. S. Sarantseva, and A. F. Starace, J. Phys. B **42**, 035601 (2009).

[53] M. V. Frolov, N. L. Manakov, A. M. Popov, O. V. Tikhonova, E. A. Volkova, A. A. Silaev, N. V. Vvedenskii, and A. F. Starace, Phys. Rev. A **85**, 033416 (2012).

[54] Y. Okajima, O. I. Tolstikhin, and T. Morishita, Phys. Rev. A **85**, 063406 (2012).

[55] M. V. Frolov, N. L. Manakov, A. A. Minina, A. A. Silaev, N. V. Vvedenskii, M. Y. Ivanov, and A. F. Starace, Phys. Rev. A **99**, 053403 (2019).

[56] X. M. Tong and C. D. Lin, J. Phys. B **38**, 2593 (2005).

[57] Y. Mairesse, A. de Bohan, L. J. Frasinski, H. Merdji, L. C. Dinu, P. Monchicourt, P. Breger, M. Kovačev, R. Taïeb, B. Carré, H. G. Muller, P. Agostini, and P. Salières, Science **302**, 1540 (2003).

[58] N. Dudovich, O. Smirnova, J. Levesque, Y. Mairesse, M. Y. Ivanov, D. M. Villeneuve, and P. B. Corkum, Nat. Phys. **2**, 781 (2006).

[59] I. P. Christov, M. M. Murnane, and H. C. Kapteyn, Phys. Rev. A **57**, R2285 (1998).

[60] E. Priori, G. Cerullo, M. Nisoli, S. Stagira, S. De Silvestri, P. Villoresi, L. Poletto, P. Ceccherini, C. Altucci, R. Bruzzese, and C. de Lisio, Phys. Rev. A **61**, 063801 (2000).

[61] M. Geissler, G. Tempea, and T. Brabec, Phys. Rev. A **62**, 033817 (2000).

[62] V. Tosa, H. T. Kim, I. J. Kim, and C. H. Nam, Phys. Rev. A **71**, 063807 (2005).

[63] V. S. Yakovlev, M. Ivanov, and F. Krausz, Opt. Express **15**, 15351 (2007).

[64] M. B. Gaarde, J. L. Tate, and K. J. Schafer, J. Phys. B **41**, 132001 (2008).

[65] C. Hernández-García, J. A. Pérez-Hernández, J. Ramos, E. C. Jarque, L. Roso, and L. Plaja, Phys. Rev. A **82**, 033432 (2010).

[66] C. Jin, A.-T. Le, and C. D. Lin, Phys. Rev. A **83**, 023411 (2011).

[67] C. Jin, A.-T. Le, and C. D. Lin, Phys. Rev. A **79**, 053413 (2009).

[68] F. Silva, S. M. Teichmann, S. L. Cousin, M. Hemmer, and J. Biegert, Nat. Commun. **6**, 6611 (2015).

[69] T. Gaumnitz, A. Jain, Y. Pertot, M. Huppert, I. Jordan, F. Ardana-Lamas, and H. J. Wörner, Opt. Express **25**, 27506 (2017).

[70] A. S. Johnson, D. R. Austin, D. A. Wood, C. Brahms, A. Gregory, K. B. Holzner, S. Jarosch, E. W. Larsen, S. Parker, C. S. Strüber, P. Ye, J. W. G. Tisch, and J. P. Marangos, Sci. Adv. **4**, eaar3761 (2018).

[71] Y. Fu, K. Nishimura, R. Shao, A. Suda, K. Midorikawa, P. Lan, and E. J. Takahashi, Commun. Phys. **3**, 92 (2020).

[72] X. Zhao, H. Wei, Y. Wu, and C. D. Lin, Phys. Rev. A **95**, 043407 (2017).

[73] C. Jin, G. Wang, H. Wei, A. T. Le, and C. D. Lin, Nat. Commun. **5**, 4003 (2014).